ARTICLES

Measurements of $\Delta\sigma_T$ in polarized-neutron–polarized-proton scattering

W. S. Wilburn,[1] C. R. Gould,[2] D. G. Haase,[2] P. R. Huffman,[1] C. D. Keith,[2] N. R. Roberson,[1] and W. Tornow[1]
[1]*Physics Department, Duke University, Durham, North Carolina 27708*
and Triangle Universities Nuclear Laboratory, Durham, North Carolina 27708
[2]*Physics Department, North Carolina State University, Raleigh, North Carolina 27695*
and Triangle Universities Nuclear Laboratory, Durham, North Carolina 27708
(Received 5 June 1995)

The spin-dependent total cross-section difference $\Delta\sigma_T$ has been measured at energies of 7.43, 9.57, and 11.60 MeV for neutrons, polarized transverse to the beam momentum, transmitted through a transversely polarized proton target. In addition, the energy at which $\Delta\sigma_T$ crosses through zero has been determined in the energy range 3.65–6.25 MeV. The measurements were carried out with a polarized TiH_2 target and polarized neutrons from the ^{3}H(**p**,**n**)^{3}He and ^{2}H(**d**,**n**)^{3}He reactions. The cross-section differences $\Delta\sigma_T$ are sensitive to the strength of the $^3S_1-{}^3D_1$ mixing parameter ϵ_1. Phase-shift analyses are used to determine ϵ_1 values from the data. The values are in good in agreement with *NN* potential models and do not support the low ϵ_1 values found in previous studies around 15–20 MeV.

PACS number(s): 21.30.+y, 13.75.Cs, 24.70.+s, 25.40.Dn

I. INTRODUCTION

In this paper we report measurements of the spin-dependent total cross-section difference $\Delta\sigma_T$ for neutrons, polarized transverse to the beam momentum, transmitted through a transversely polarized proton target. The measurements are part of a Triangle University Nuclear Laboratory (TUNL) program that seeks to determine unambiguously the low-energy phase-shift parameters for neutron-proton scattering. In the range 1–20 MeV, the three most important *n-p* phase-shift parameters are $^1S_0$, $^3S_1$, and the tensor force parameter ϵ_1, the isoscalar $^3S_1-{}^3D_1$ mixing parameter. Prediction of these phase shifts from realistic meson-exchange models, or from quark models is central to a quantitative understanding of the nucleon-nucleon (*NN*) force [1–4].

While the last few years have seen considerable progress in parameterizing nucleon-nucleon (*NN*) scattering data in terms of phase shifts [5,6], the present data base is still not sufficient to determine $^1S_0$, $^3S_1$, and ϵ_1 uniquely. As we discuss below, three independent observables are needed to do this, for example, σ_0, the total *n-p* cross section; $\Delta\sigma_T$, the transverse spin-spin cross section; and $\Delta\sigma_L$, the longitudinal spin-spin cross section. Since the latter two involve polarized beams and polarized targets, the measurements are difficult. Only in the last ten years has it been possible to carry out precision measurements of one or the other of these two observables [7,8]. Until recently there were no $\Delta\sigma_L$ data below 50 MeV and no $\Delta\sigma_T$ data below 350 MeV. As a result, ϵ_1 is surprisingly poorly known, and the strength of the *NN* tensor force continues to be controversial [5,9–12].

The measurements reported here were carried out in two different energy regions: the first around 5 MeV, where potential models predict $\Delta\sigma_T$ is changing rapidly and crossing through zero, and the second at energies around 10 MeV, where $\Delta\sigma_T$ changes relatively slowly with energy. The advantage of a zero-crossing measurement is that it is relatively insensitive to systematic errors in beam and target polarization. On the other hand, the polarized neutron fluxes available from the ^{3}H(**p**,**n**)^{3}He reaction in this energy range are low, and this limits the statistical accuracy of any one measurement. The higher energy measurements can be carried out with high statistical accuracy using the intense ^{2}H(**d**,**n**)^{3}He source reaction but are limited in precision by the absolute accuracy with which the beam and target polarizations and the target thickness can be measured.

The outline of the paper is as follows: In Sec. II the principles of the measurements are discussed, especially emphasizing the sensitivity of both $\Delta\sigma_T$ and $\Delta\sigma_L$ to ϵ_1, and the insensitivity of these quantities to the $^1P_1$ phase shift (which has traditionally complicated extraction of ϵ_1 from other spin-correlation measurements). In Sec. III we discuss the experimental details of our polarized proton target, and our polarized neutron beam facility. Sections IV and V present the analysis of our data and results. Finally, in Sections VI and VII, we present comparisons of our data to current theoretical predictions and conclusions based on the present work. A preliminary version of this work has been published previously [13].

II. PRINCIPLES OF MEASUREMENT

The spin-dependent total cross-section differences are defined as the differences in the total cross sections with neutrons and protons polarized antiparallel and parallel to each other and either longitudinal (L) or transverse (T) to the beam direction:

$$\Delta\sigma_L=\sigma(\rightleftarrows)-\sigma(\rightrightarrows) \tag{1}$$

and

$$\Delta\sigma_T=\sigma(\uparrow\downarrow)-\sigma(\uparrow\uparrow), \tag{2}$$

where the top (first) arrow refers to the proton and the bottom (second) arrow to the neutron spin orientation.

The total cross section is written as the sum of a spin-independent term σ_0 and a spin-dependent term σ_s:

$$\sigma=\sigma_0+\sigma_s. \tag{3}$$

The spin-dependent term changes sign between parallel and antiparallel orientations, and consists of central σ_c and tensor σ_t contributions:

$$\sigma_s=\sigma_c(\boldsymbol{\sigma}_1\cdot\boldsymbol{\sigma}_2)+\sigma_t S_{12}, \tag{4}$$

where $\boldsymbol{\sigma}_1$ and $\boldsymbol{\sigma}_2$ are unit vectors along the spin directions of the two nucleons, and

$$S_{12}=3(\boldsymbol{\sigma}_1\cdot\hat{\mathbf{r}})(\boldsymbol{\sigma}_2\cdot\hat{\mathbf{r}})-\boldsymbol{\sigma}_1\cdot\boldsymbol{\sigma}_2 \tag{5}$$

has the same angular dependence as the tensor force operator. The unit vector $\hat{\mathbf{r}}$ is along the direction $\mathbf{r}$ connecting the two nucleons. Therefore,

$$\Delta\sigma_L=-2(\sigma_c+2\sigma_t) \tag{6}$$

and

$$\Delta\sigma_T=-2(\sigma_c-\sigma_t). \tag{7}$$

In 1980 Bugg pointed out that the uncertainty in the phase-shift parameters ϵ_1 and $^1P_1$ at 25 and 50 MeV could be reduced if in addition to the spin-correlation coefficient $A_{zz}(\theta)$, data for the spin-dependent longitudinal neutron-proton total cross section difference $\Delta\sigma_L$ were available [14]. A few years later, it was shown in Refs. [15,16] that at lower energies $\Delta\sigma_L$ and the transverse neutron-proton total cross-section difference $\Delta\sigma_T$ are considerably more sensitive to ϵ_1 than at 25 or 50 MeV. In addition, the sensitivity of these observables to $^1P_1$ is greatly reduced at low incident neutron energies.

The solid curves in Fig. 1 represent the energy dependence of $\Delta\sigma_L$ (left-hand side) and $\Delta\sigma_T$ (right-hand side) in the energy range below $E_n=30$ MeV.[1] Both $\Delta\sigma_L$ and $\Delta\sigma_T$ are negative, except at very low energies. The zero crossings are of special interest and will be discussed later. The dashed curves correspond to a $\pm1°$ change in ϵ_1. Both $\Delta\sigma_L$ and $\Delta\sigma_T$ display considerable sensitivity to variations in ϵ_1 at low energies. However, this sensitivity decreases quite rapidly with increasing neutron energy, i.e., $\partial(\Delta\sigma_L)/\partial\epsilon_1$ decreases from 60 mb/deg at 4 MeV to 8 mb/deg at 50 MeV.[2] As can be seen from Fig. 1, the sensitivity of $\Delta\sigma_T$ to ϵ_1 is a factor of 2 smaller than the sensitivity found for $\Delta\sigma_L$. This observation follows directly from the definition of S_{12}. In the case of the longitudinal spin orientation, S_{12} simplifies to

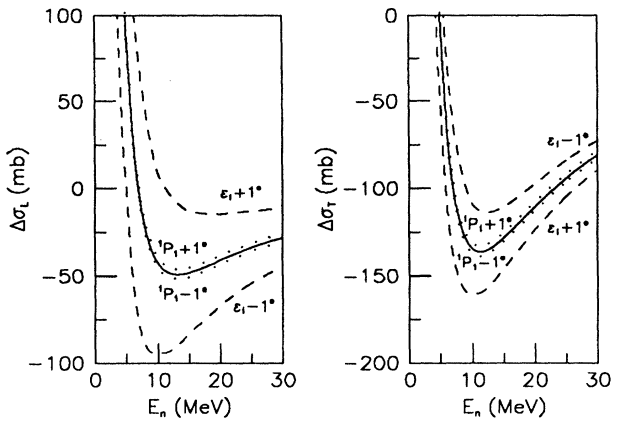

FIG. 1. Spin-dependent total cross-section differences $\Delta\sigma_L$ (left) and $\Delta\sigma_T$ (right) as predicted by the VPI SM94 phase-shift analysis [6]. The dashed curves show sensitivities to $\pm1°$ changes in ϵ_1. The dotted curves show sensitivities to $\pm1°$ changes in $^1P_1$.

$S_{12}^L=2\boldsymbol{\sigma}_1\cdot\boldsymbol{\sigma}_2=2$, compared to $S_{12}^T=-\boldsymbol{\sigma}_1\cdot\boldsymbol{\sigma}_2=-1$ for the transverse orientation. The opposite signs obtained for S_{12}^L and S_{12}^T are responsible for the fact that an increase of ϵ_1 alters the magnitude of $\Delta\sigma_L$ and $\Delta\sigma_T$ in opposite directions, as observed in Fig. 1.

In contrast to the spin-correlation coefficients $A_{zz}(\theta)$ and $A_{yy}(\theta)$, which are, except for $\theta_{\text{c.m.}}=90°$, sensitive to both ϵ_1 and $^1P_1$, the spin-dependent total cross-section differences $\Delta\sigma_L$ and $\Delta\sigma_T$ do not depend strongly on $^1P_1$ at low energies. As shown in Fig. 1, the sensitivity to a $\pm1°$ change of $^1P_1$ has only a very small influence on $\Delta\sigma_L$ and $\Delta\sigma_T$ near 10 MeV. Of course, with increasing neutron energy, the contribution of $^1P_1$ becomes more important.

The surprisingly large sensitivity of $\Delta\sigma_L$ and $\Delta\sigma_T$ to variations of ϵ_1 is due to cancellations between individual phase shifts, which contribute to the observables at low energies. The expressions for $\Delta\sigma_L$ and $\Delta\sigma_T$ in terms of NN phase shifts are

$$\begin{aligned}\Delta\sigma_L=\frac{2\pi}{k^2}\{&\sin^2\delta(^1S_0)+\sin^2\delta(^3P_0)+3\sin^2\delta(^1P_1)\\&-3\sin^2\delta(^3P_1)-\cos(2\epsilon_1)[\sin^2\delta(^3S_1)-\sin^2\delta(^3D_1)]\\&+2\sqrt{2}\sin(2\epsilon_1)\sin[\delta(^3S_1)+\delta(^3D_1)]\}\end{aligned} \tag{8}$$

and

$$\begin{aligned}\Delta\sigma_T=\frac{2\pi}{k^2}\{&\sin^2\delta(^1S_0)-\sin^2\delta(^3P_0)+3\sin^2\delta(^1P_1)-3\sin^2\epsilon_1\\&-\cos(2\epsilon_1)[\sin^2\delta(^3S_1)+2\sin^2\delta(^3D_1)]\\&-\sqrt{2}\sin(2\epsilon_1)\sin[\delta(^3S_1)+\delta(^3D_1)]\},\end{aligned} \tag{9}$$

where k is the wave number, and phase shifts with total angular momentum $J\geq2$ are neglected, since their influence is negligible in the energy region of interest. Using the VPI SM94 n-p phase-shift solution at $E_n=10$ MeV, Eq. (8) gives

[1]The curves were calculated with the code SAID of the Virginia Polytechnic Institute and State University (VPI) group [6]. The n-p phase-shift solution SM94 was used.

[2]Similar studies were done with the Bonn B and Paris NN potential. The sensitivity results are essentially independent of the specific potential or phase-shift solution.

$$\Delta\sigma_L=\frac{\pi}{k^2}(5.5361\sin 2\epsilon_1-0.389\,62). \tag{10}$$

Therefore, a 1° change of ϵ_1 corresponds to a 120% change in $\Delta\sigma_L$. As stated earlier, the sensitivity of $\Delta\sigma_T$ to ϵ_1 is half as large.

The experimental determination of $\Delta\sigma_T$ ($\Delta\sigma_L$) requires the measurement of the difference in the attenuation of a transversely (longitudinally) polarized neutron beam through a transversely (longitudinally) polarized proton target when one or the other spin is reversed.

Let N_0 be the number of neutrons, polarization P_n, incident on a proton target, polarization P_t. Then the number of neutrons detected behind the target for parallel and antiparallel spin orientation is

$$N^{\rm p}=\eta N_0 e^{-x\sigma^{\rm p}}, \tag{11}$$

$$N^{\rm ap}=\eta N_0 e^{-x\sigma^{\rm ap}}. \tag{12}$$

Here, η is the detector efficiency, x is the number of protons per cm^2, and $\sigma^{\rm p}$ and $\sigma^{\rm ap}$ are the neutron-proton total cross sections for parallel and antiparallel spin orientations. The cross sections are given by

$$\sigma^{\rm p}=\sigma_0-\tfrac{1}{2}P_tP_n\Delta\sigma, \tag{13}$$

$$\sigma^{\rm ap}=\sigma_0+\tfrac{1}{2}P_tP_n\Delta\sigma, \tag{14}$$

where $\Delta\sigma$ is $\Delta\sigma_L$ or $\Delta\sigma_T$.

The spin-dependent total cross-section difference can be extracted from the asymmetry measured with parallel and antiparallel neutron spin orientation:

$$\varepsilon=\frac{N^{\rm p}-N^{\rm ap}}{N^{\rm p}+N^{\rm ap}}=\frac{e^{(-x\sigma_0+xP_tP_n\Delta\sigma/2)}-e^{(-x\sigma_0-xP_tP_n\Delta\sigma/2)}}{e^{(-x\sigma_0+xP_tP_n\Delta\sigma/2)}+e^{(-x\sigma_0-xP_tP_n\Delta\sigma/2)}}$$

$$=\tanh\left(\frac{xP_tP_n\Delta\sigma}{2}\right). \tag{15}$$

Since $xP_tP_n\Delta\sigma/2$ is less than 5×10^{-3} in the 5–30 MeV energy range for the target used in this experiment, the hyperbolic tangent can be replaced by its argument, and therefore the asymmetry measured with longitudinal spin orientation is

$$\varepsilon_L=\tfrac{1}{2}xP_tP_n\Delta\sigma_L \tag{16}$$

and for the asymmetry measured with transverse spin orientation

$$\varepsilon_T=\tfrac{1}{2}xP_tP_n\Delta\sigma_T. \tag{17}$$

The error introduced by this approximation is less than 0.1% in all cases.

In order to extract $\Delta\sigma_L$ and $\Delta\sigma_T$ from Eqs. (16) and (17), x, P_t, and P_n must be known accurately, except at or near the zero-crossing energies of $\Delta\sigma_L$ and $\Delta\sigma_T$. The asymmetries ε_L and ε_T are zero at these energies, independent of the magnitude of x, P_t, and P_n. The determination of the exact zero-crossing energies is limited primarily by statistical uncertainties.

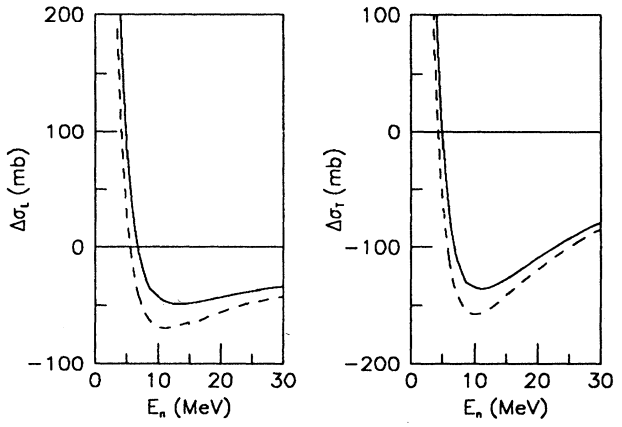

FIG. 2. Predictions for the spin-dependent total cross-section differences $\Delta\sigma_L$ (left) and $\Delta\sigma_T$ (right) from the Bonn B [18] (solid) and Paris [20] (dashed) potential models.

Figure 2 presents the predictions of the Bonn B and Paris potential models for $\Delta\sigma_L$ (left) and $\Delta\sigma_T$ (right). These predictions are chosen as representative of modern n-p and p-p potential models, respectively. Sizeable differences exist between the two predictions, especially in the 5–20 MeV energy range. As has been pointed out in Ref. [16], these differences are only partially related to differences in the values for ϵ_1. Like all n-p observables used in the past for determining ϵ_1 (i.e., A_{yy}, A_{zz}, and $K_y^{y'}$), $\Delta\sigma_L$ and $\Delta\sigma_T$ are sensitive to the angular momentum $\ell=0$ NN phase shifts, $^1S_0$ and $^3S_1$. It is common practice to assume that these phase shifts are well determined.

The $^1S_0$ NN force component of the Bonn potentials [17,18] is fitted to the n-p $^1S_0$ scattering length (present recommended value $a_{np}=-23.748\pm0.009$ fm [19]). However, the $^1S_0$ NN force component of the Paris potential [20] is fitted to the p-p $^1S_0$ scattering length (present recommended value $a_{pp}=-17.3\pm0.4$ fm [19]). Therefore, the associated values for the $^1S_0$ phase shift are different at low energies. This is the main reason for the large differences between $\Delta\sigma_L$ and $\Delta\sigma_T$ for the Bonn B potential and the Paris potential.

A comparison of zero-crossing energies of $\Delta\sigma_L$ and $\Delta\sigma_T$ restricted to n-p potentials and n-p phase-shift analyses is shown in Fig. 3. The new Nijmegen potential[3] Nijm93 [2] and the new Argonne potential AV18 [21] employ charge-independence breaking in the $^1S_0$ NN state. The variance in the predicted zero-crossing energies is not large, in agreement with the expectation that ϵ_1 at very low energies is constrained by the quadrupole moment of the deuteron. However, this theoretical expectation has never been verified experimentally. With this fact in mind, zero-crossing measurements of $\Delta\sigma_L$ and $\Delta\sigma_T$ are very important. They are a stringent test of the meson-exchange picture of the NN interaction. In contrast to the situation at higher energies,

[3]Phase-shift parameters and predictions of observables for the Nijmegen phase-shift analysis and potential model were obtained using the Nijmegen NN online analysis code.

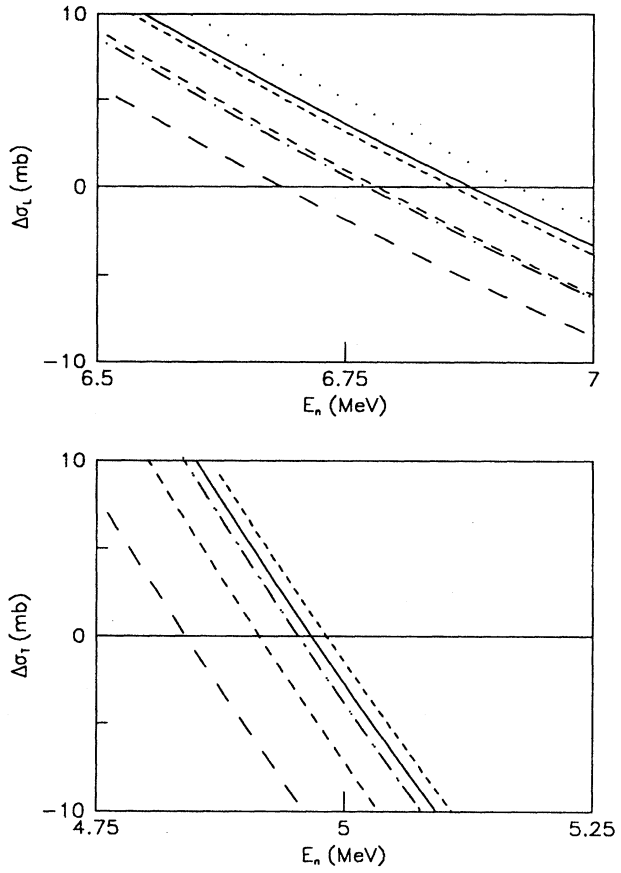

FIG. 3. Expanded view of predictions for the zero crossings of $\Delta\sigma_L$ (top) and $\Delta\sigma_T$ (bottom). Shown are the n-p phase-shift analyses PWA93 [5] (solid) and SM94 [6] (dotted), and the n-p potential models AV18 [21] (dot-dashed), Bonn B [18] (medium dashed), full Bonn [17] (long dashed), and Nijm93 [2] (short dashed).

where a large number of partial waves contribute to the observable, only three NN force components ($^1S_0$, $^3S_1$, and ϵ_1) are important in the zero-crossing energy region.

Now let us return to the discussion of low-energy $\Delta\sigma_L$ and $\Delta\sigma_T$ experiments and their importance for the NN tensor force. In general, all observables that are sensitive to ϵ_1 are also sensitive to the singlet NN force components. This sensitivity is due to the spin-dependent central part of $\Delta\sigma_L$ and $\Delta\sigma_T$ and not due to the tensor force. Therefore, the influence of the singlet NN force components subtracts out completely in the difference $\Delta=\Delta\sigma_L-\Delta\sigma_T$:

$$\Delta=\frac{2\pi}{k^2}\{2\sin^2\delta(^3P_0)-3\sin^2\delta(^3P_1)+3\sin^2\epsilon_1 +3\cos(2\epsilon_1)\sin^2\delta(^3D_1) +3\sqrt{2}\sin(2\epsilon_1)\sin[\delta(^3S_1)+\delta(^3D_1)]\}. \quad (18)$$

As can be seen, Δ depends only on the triplet phase shifts and the mixing parameter ϵ_1. Figure 4 demonstrates the sensitivity of Δ to a $\pm 1^\circ$ change in ϵ_1.

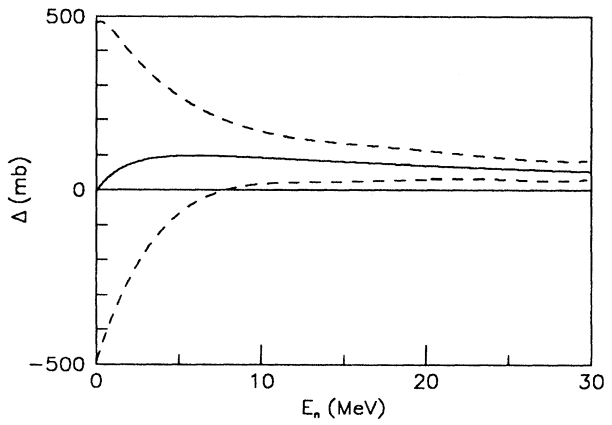

FIG. 4. Prediction of $\Delta=\Delta\sigma_L-\Delta\sigma_T$ from the VPI SM94 [6] phase-shift analysis. The dashed curves show sensitivities to $\pm 1^\circ$ changes in ϵ_1.

III. EXPERIMENTAL DETAILS

A. Polarized target

The target material consisted of titanium hydride (TiH_2). The protons of the TiH_2 were statically polarized at a temperature of 13 mK in an external field of 7 T produced by a superconducting magnet. The cryostat and refrigerator used for this work have been previously described [22]. The TUNL TiH_2 target is similar to a target built at the Kernforschungzentrum Karlsruhe [23,24]. The TiH_2 powder was compressed into a rectangular copper box at a pressure of 1.5 GPa to form a dense solid. The box was made from 2 mm copper plate with front and back faces open so that neutrons did not pass through the copper, which was also polarized. The box was mounted by a squeeze connector on the copper cold finger of the dilution refrigerator. The temperature was measured by a ^{60}CoCo thermometer and two ^{3}He melting curve thermometers, which were thermally anchored to the copper collar [25]. The TiH_2 target has a density of 3.75 g/cm^3 and a thickness of 22.4 mm, giving a proton thickness of 0.203 b^{-1}. The open area of the TiH_2 face is 14.0 mm $\times$34.1 mm ($w\times h$).

We found, as did the Karlsruhe group, that commercial TiH_2 powder acts as an electrical and thermal insulator when compressed. The measured electrical conductivity of our compressed commercial TiH_2 samples decreased with decreasing temperature, an effect we attribute to surface impurities on the grains. The Wiedemann-Franz relation implies that such samples have low thermal conductivity at low temperatures, and in fact a target made from such powder could not be cooled below 50 mK in our refrigerator even though the copper collar was at 13 mK. We finally compressed a target from TiH_2 powder produced at Karlsruhe, which showed the proper metallic conductivities and cooled to 13 mK.

In principle, the polarization of the target can be calculated from the temperature and magnetic field. However, temperature measurements were considered unreliable because of the low thermal conductivity of the TiH_2. The polarization of the target was instead determined by measure-

ment of the spin-dependent transmission asymmetry $\varepsilon_T = \frac{1}{2} x P_t P_n \Delta\sigma_T$ for 1.94 MeV neutrons (see Sec. IV C). Since the uncertainty in $\Delta\sigma_T$ is small at this energy, the asymmetry measurement provides a determination of xP_t averaged over the area of the target illuminated by the neutron beam.

The target could be cooled from 4 K to the polarized state in 24 h. The target was always cooled at least 48 h prior to the start of an experiment to assure that thermal equilibrium was reached. The target was also periodically warmed to 1 K to measure neutron transmission through unpolarized TiH_2.

B. Polarized beam

Polarized neutrons were produced by polarization-transfer reactions using primary beams of either polarized protons or deuterons. For neutron energies below 7 MeV the ^{3}H(**p**,**n**)^{3}He reaction was used because the negative Q value of 0.764 MeV makes it possible to reach low energies. Above 7 MeV, the ^{2}H(**d**,**n**)^{3}He reaction with a 3.269 MeV positive Q value was used. Since safety considerations limit the thickness of tritium targets, the second reaction was used whenever possible to obtain higher neutron fluxes.

1. General

The polarized charged-particle beams were produced by the TUNL atomic beam polarized ion source [26] and accelerated by an FN tandem accelerator. The beam was momentum analyzed by a 59° bending magnet and was directed onto the neutron production target by an additional 20° bending magnet. The position of the beam in the horizontal and vertical planes was stabilized by four slit-current feedback systems. In addition, the centroid of the beam was obtained from a wire scanner and used to make corrections to the beam position every 2 s. The last 2 m of beam pipe were made of iron with two layers of high permeability alloy inside to prevent deflection of the beam by the magnetic field of the polarized proton target.

The charged-particle beam is initially produced at the exit of the polarized ion source with a longitudinal polarization. A Wien filter spin precessor was used to change this direction so that the polarization was transverse at the neutron production target. The polarization direction was reversed at a rate of 10 Hz by alternately turning on two radio frequency atomic transition units in the source. The polarization of the charged-particle beam was monitored by a carbon-foil polarimeter placed in the beam line before the 20° magnet. The polarimeter uses two silicon surface barrier detectors placed symmetrically about the beam at $\pm 40°$.

The neutron beam was defined by a 60 cm polyethylene collimator placed after the polarized proton target. The collimator bore is rectangular in cross section and tapered to view an area of the target measuring 9.4 mm$\times$25.7 mm ($w \times h$). A small copper preshield was placed between the neutron production target and the polarized target to reduce the number of neutrons hitting the superconducting magnet and other parts of the cryostat. The alignment of the detector with the polarized target was verified by exposing x-ray films to the gammas produced in the neutron production target. The main neutron detectors were located in a large polyethylene shield after the collimator. Figure 5 shows the experimental apparatus.

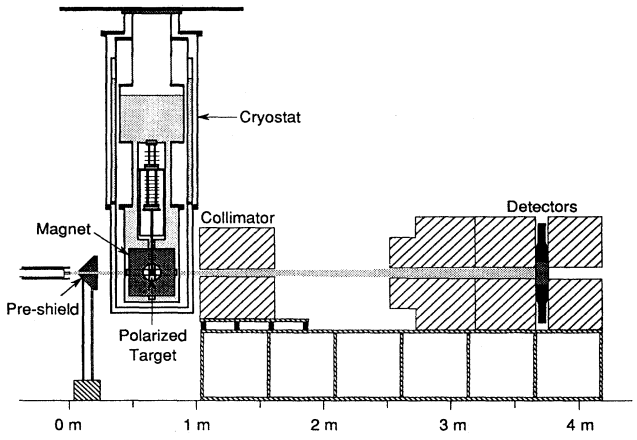

FIG. 5. Diagram of the experimental apparatus showing the polarized target, collimation, and neutron detectors.

2. Neutrons produced by ^{3}H(p,n)^{3}He

Polarized neutron beams with energies below 7 MeV were produced by bombarding a tritiated-titanium target with polarized protons. A ^{4}He gas cell with a 2.5 μm Havar entrance foil surrounding the tritium target prevents contamination of the beam line. The proton beam was stopped in the tritium foil backing, which in most cases consisted of 0.5 mm ^{58}Ni. This material was chosen because of its 9.44 MeV threshold for proton-induced neutron production. A copper backing was also used at the lowest energy where this was not a concern. The neutron flux was monitored by charge integration of the incident protons.

The proton beam polarization was determined from published analyzing powers for elastic scattering from carbon [27,28]. Neutron polarizations were obtained through the polarization transfer coefficient $K_y^{y'}$ for the neutron production reaction, which has been previously measured [29,30]. In addition, $K_y^{y'}$ was measured at neutron energies of 1.94, 5.21, and 5.81 MeV using a neutron polarimeter [31,32]. These measurements were made both to extend the lower range of measured values and to verify the earlier results.

Neutron energies were determined by observing resonances in the total cross sections of carbon at 2.077, 2.950, and 6.293 MeV and of oxygen at 4.835 and 5.052 MeV. Neutron time-of-flight measurements were made using pulsed beam to determine neutron backgrounds and to set detector thresholds.

3. Neutrons produced by ^{2}H(d,n)^{3}He

Polarized neutron beams with energies above 6 MeV were produced by bombarding a deuterium gas cell with polarized deuterons. Although the deuteron beam was nominally vector polarized, there was also a small tensor component. The deuterium cell was 6 cm long and was operated at a pressure of 4 bar. The gas was contained by a 10 μm Havar entrance foil. The deuterons were stopped by a tantalum disk at the back of the cell. Since the neutron yield is affected by the tensor deuteron polarization, beam current integration is not sufficient for accurate flux normalization. Instead, a neutron monitor was used at zero degrees.

The neutron monitor detector is a small scintillator cell (25 mm×11 mm×22 mm) ($l \times w \times h$) filled with Nuclear Enterprises liquid scintillator, NE–213. The cell was placed between the neutron preshield and the polarized target. The light of scintillation is coupled to a 51 mm photomultiplier tube through a ~1 m light guide. This arrangement allows the photomultiplier tube to be placed a safe distance from the polarizing magnet of the target. A cylinder of high-permeability alloy was placed around the tube as a magnetic shield. The anode signal of the neutron monitor was analyzed by a discriminator. No pulse-shape discrimination was needed, since the efficiency for detecting gammas in such a thin detector with our high discriminator threshold is negligible.

The deuteron vector polarization was monitored by the $^{12}C(\mathbf{d},p_0)^{13}C$ reaction in the charged-particle polarimeter. The neutron polarization was obtained by calibrating the asymmetry for this reaction against a neutron polarimeter [31,32]. The polarization transfer coefficient for the neutron production reaction is implicitly included in this calibration.

The main neutron detectors were two liquid organic scintillators (Bicron, BC–501) contained in aluminum cylinders measuring 127 mm×127 mm ($d \times h$). The light of scintillation passes through glass windows and is detected by 127 mm diameter photomultiplier tubes. The detectors were placed together at zero degrees with the axis of the photomultiplier tubes vertical. The detectors were shielded from magnetic fields by individual shields of high-permeability alloy and a pipe of soft iron. The entire assembly was placed inside a large polyethylene neutron shield located 3.35 m from the polarized target.

Anode signals from the main detectors were analyzed by pulse-shape discrimination (PSD) [33]. Since the dead time of the system is dominated by the 300 ns required for PSD, dead-time corrections were calculated using the live-time signal of the PSD module.

C. Data acquisition

The spin direction of the neutron beam was reversed at a rate of 10 Hz according to the eight-step sequence $+--+-++-$, where + and − refer to neutron polarization parallel and antiparallel to the proton target polarization, respectively. This spin-reversal sequence cancels detector gain drifts to quadratic order [34]. All data were read into Camac scalers connected to the online computer. A veto signal was generated for each spin flip to inhibit data collection. The veto signal started 2 ms before and lasted until 5 ms after the spin flip. During this time, the scalers were read and the data routed by spin to time-ordered spectra. Each point along the x axis of the spectra corresponds to one eight-step sequence, allowing the data to be manipulated in 800 ms time slices.

Since pulse-shape discrimination for the main detectors was performed in hardware, the data were counted by scalers. Signals from the polarimeter detectors were amplified and converted to scaler counts by single-channel analyzers. In addition, counts from the beam current integrator and a 100 kHz pulser were recorded. Dead-time signals were generated for the main detector by performing a logical AND operation between the pulser signal and the live-time outputs of the PSD modules. Beam profiles for both spin states were stored.

Data were collected at each energy with the target cold, starting at 1.94 MeV to determine the target polarization and thickness. The target was then warmed to ~1 K and a roughly equal amount of data was collected for each energy with the target unpolarized. Proton beam polarizations were measured every few hours, while deuteron beam polarizations were monitored continuously.

IV. DATA ANALYSIS

A. Neutron transmission asymmetries

The first step in calculating neutron transmission asymmetries was the elimination of bad sequences from the data set. Eight-step sequences were removed when the number of counts from the 100 kHz pulser differed by more than four standard deviations from the nominal value. This condition occurs when data collection is externally inhibited because the beam current is outside of allowable limits. Typically, less than 1% of the data were rejected.

Neutron transmission asymmetries for both main detectors were calculated for each 800 ms eight-step sequence according to

$$\varepsilon_T = \frac{N_+ - N_-}{N_+ + N_-}, \tag{19}$$

where $N_\pm$ is the number of neutron counts in each spin state normalized to the incident flux and corrected for dead time. All asymmetries for a given measurement were then combined in a statistically weighted average. Both statistical uncertainties and standard deviations were calculated for the average asymmetries. The degree of agreement between these two quantities (see Sec. V) gives a measure of the nonstatistical fluctuations in the asymmetries.

For each energy, neutron asymmetries for both polarized target and unpolarized target are normalized to their respective beam polarimeter asymmetries and subtracted to remove systematic errors, for instance, these due to analyzing power effects in the neutron production reaction. This is given by

$$\bar{\varepsilon}_T/\bar{\varepsilon}_p = (\bar{\varepsilon}_T/\bar{\varepsilon}_p)_c - (\bar{\varepsilon}_T/\bar{\varepsilon}_p)_w, \tag{20}$$

where $\bar{\varepsilon}_T$ is the average neutron asymmetry, $\bar{\varepsilon}_p$ is the average polarimeter asymmetry, and the subscripts c and w refer to cold (polarized) and warm (unpolarized) target respectively.

B. Beam polarization

The neutron beam polarization was determined from the left-right counting asymmetry in the charged-particle polarimeter. Systematic effects are cancelled by taking the difference between asymmetries for the two spin states ($\pm$)

$$\varepsilon_p = \frac{\varepsilon_{p+} - \varepsilon_{p-}}{2}. \tag{21}$$

Since the polarimeter was located before the final bending magnet, the beam polarization direction was not completely transverse at this point and the polarimeter asymmetry must be divided by $\cos(\Delta\theta)$, where $\Delta\theta$ is the polarization angle with respect to the transverse direction. Knowing the analyz-

TABLE I. Potential model and phase-shift analysis predictions for $\Delta\sigma_T$ at $E_n = 1.94$ MeV.

	$\Delta\sigma_T$ (mb)
Argonne AV18[a]	915.6
Bonn B[b]	913.4
Full Bonn[c]	913.2
Nijmegen Nijm93[d]	916.6
Nijmegen PWA93[e]	915.0
VPI SM94[f]	917.9

[a]Reference [21].
[b]Reference [18].
[c]Reference [17].
[d]Reference [2].
[e]Reference [5].
[f]Reference [6].

ing power A_y for the polarimeter reaction and the polarization transfer coefficient $K_y^{y'}$ for the neutron production reaction allows the neutron beam polarization to be calculated:

$$P_n = \frac{K_y^{y'}\varepsilon_p}{A_y \cos(\Delta\theta)}. \tag{22}$$

For a proton beam, these values are known from published measurements and from auxiliary neutron polarization measurements. In the case of a deuteron beam, the effective charged-particle polarimeter analyzing powers $A_y^{\text{eff}} = A_y / K_y^{y'}$ have been measured.

C. Target polarization and thickness

The product of polarization and thickness for the polarized proton target was obtained by measuring the neutron transmission asymmetry at 1.94 MeV and normalizing to the value of $\Delta\sigma_T$ obtained from the Nijmegen phase-shift analysis PWA93 [5]. At this energy, $\Delta\sigma_T$ is constrained by kinematics and the properties of the deuteron [35]. Calculations made from n-p potential models and phase-shift analyses, shown in Table I, agree to approximately $\pm 0.2\%$. The primary uncertainty comes from the accuracy of the neutron energy calibration, which is estimated to be ± 20 keV. Based on these considerations, we adopt a value of 915 ± 17 mb at 1.94 MeV. The uncertainty in this value is estimated by adding in quadrature the effect of the neutron energy uncertainty and the estimated uncertainty in the theoretical value. In addition, the target thickness was measured by weighing, which allowed the target polarization to be known independently.

TABLE II. Corrections C_1 and C_2 applied to the neutron polarization for $E_n < 7$ MeV, as described in the text.

E_n (MeV)	C_1	C_2
1.94	0.978	1.000
3.65	0.984	0.929
4.42	0.986	0.690
4.91	0.987	0.667
5.21	0.988	0.654
5.81	0.989	0.752
6.25	0.989	0.699

D. Corrections to the data

Three corrections have been applied to the neutron polarizations used in analyzing the data. Two corrections are relevant only to the ^{3}H(**p**,**n**)^{3}He configuration, while the third only applies to data taken with the ^{2}H(**d**,**n**)^{3}He source reaction.

Although the magnetic field used to polarize the proton target is nominally parallel to the neutron polarization direction, it is possible for fringing fields to precess the neutrons spins. This precession reduces the average neutron polarization by the factor C_1. These are obtained from Monte Carlo calculations and given in Table II.

Since for safety considerations relatively little tritium is used for producing neutrons, neutrons produced by other reactions can produce a significant background. These backgrounds have been measured by time-of-flight techniques. In addition, studies with the neutron polarimeter indicate that this background is not significantly polarized. The effect of the unpolarized background is to reduce the neutron polarization by the factor C_2, given in Table II. The corrections are large, but it should be emphasized that they only apply to the data used in determining the $\Delta\sigma_T$ zero crossing, which are insensitive to such effects.

Although the deuteron beam nominally has no tensor polarization, in practice there was a small component, as mentioned earlier. Since the tensor polarization was different between the $\Delta\sigma_T$ measurements and the polarimeter calibration, we corrected the analyzing power of the polarimeter above 7 MeV by multiplying by $C_3 = 1.009$, a factor estimated from known ^{12}C(**d**,p)^{13}C tensor analyzing powers.

E. $\Delta\sigma_T$

Values of $\Delta\sigma_T$ were obtained from Eq. (20) at each energy by applying the appropriate normalizations and multiplicative corrections. For $E_n < 7$ MeV, $\Delta\sigma_T$ is given by

$$\Delta\sigma_T(E) = \left\{ \left[\frac{A_y(E)}{A_y(E_0)} \right] \left[\frac{C_1(E_0)C_2(E_0)}{C_1(E)C_2(E)} \right] \left[\frac{K_y^{y'}(E_0)}{K_y^{y'}(E)} \right] \Delta\sigma_T(E_0) \right\} \frac{\bar{\varepsilon}_T(E)/\bar{\varepsilon}_p(E)}{\bar{\varepsilon}_T(E_0)/\bar{\varepsilon}_p(E_0)}, \tag{23}$$

where E is the neutron energy of interest and $E_0 = 1.94$ MeV, the neutron energy at which xP_t was determined. For $E_n > 7$ MeV, $\Delta\sigma_T$ is given by

$$\Delta\sigma_T(E) = \left\{ \left[\frac{A_y^{\text{eff}}(E)}{A_y(E_0)} \right] \left[\frac{\cos(\Delta\theta_d)}{\cos(\Delta\theta_p)} \right] \left[\frac{C_1(E_0)C_2(E_0)}{C_3} \right] K_y^{y'}(E_0)\Delta\sigma_T(E_0) \right\} \frac{\bar{\varepsilon}_T(E)/\bar{\varepsilon}_p(E)}{\bar{\varepsilon}_T(E_0)/\bar{\varepsilon}_p(E_0)}, \tag{24}$$

TABLE III. Cold asymmetries. Measured neutron transmission asymmetries with the proton target polarized. The uncertainties represent counting statistics, while $\sigma_{\bar{\varepsilon}_T}$ are the reduced standard deviations for N eight-step sequences, each lasting 800 ms.

E_n (MeV)	Set	N	$\bar{\varepsilon}_T$ (10^{-4})	$\sigma_{\bar{\varepsilon}_T}$ (10^{-4})
1.94	A	47 174	179.6±4.36	4.52
	B	48 651	−115.0±5.06	5.27
	C	49 428	−177.1±6.26	6.89
	D_1	39 448	−107.2±4.18	4.42
	D_2	7 127	−114.4±9.97	11.03
	E	59 969	−145.5±2.42	2.91
3.65	C	57 865	−33.81±3.22	3.31
	D	20 263	−25.99±6.29	6.46
4.42	A	63 316	7.45±2.74	2.75
4.91	A	66 302	1.54±2.83	2.85
5.21	D_1	44 931	0.72±5.08	5.14
	D_2	185 087	−0.06±1.39	1.41
5.81	A	47 236	−4.83±3.00	3.03
6.25	B	42 061	6.24±5.54	5.59
	C	142 101	5.06±2.33	2.36
7.43	E	39 336	11.71±0.68	0.68
9.57	E	62 682	16.04±0.57	0.57
11.60	E	52 242	19.08±0.71	0.71

where $\Delta\theta_p$ and $\Delta\theta_d$ refer to the proton and deuteron beams, respectively (see Sec. IV B). The zero crossing of $\Delta\sigma_T$ was determined by starting with a theoretical prediction (Bonn B) for $\Delta\sigma_T$ and performing the transformation $E \rightarrow a + bE$ to obtain the best fit to the experimental data in the zero-crossing region. This procedure holds the shape of the $\Delta\sigma_T$ curve constant, while the zero crossing is varied and was found to be insensitive to the initial theoretical prediction chosen.

V. RESULTS

Data were taken in five sets, which are designated A–E. A proton beam was used as the primary beam for sets A–D, while the data taken in set E used a deuteron beam as the primary beam. In cases where a measurement was repeated within one set, a subscript is added to distinguish the two.

TABLE IV. Warm asymmetries. Measured neutron transmission asymmetries with the proton target unpolarized. The uncertainties represent counting statistics, while $\sigma_{\bar{\varepsilon}_T}$ are the reduced standard deviations for N eight-step sequences, each lasting 800 ms.

E_n (MeV)	Set	N	$\bar{\varepsilon}_T$ (10^{-4})	$\sigma_{\bar{\varepsilon}_T}$ (10^{-4})
1.94	A	37 624	−7.21±4.94	5.12
	C	54 789	20.21±5.92	6.70
	D	47 699	4.54±4.06	4.80
	E	46 670	3.12±3.21	3.68
3.65	C	67 179	4.76±2.92	2.98
	D	23 126	3.60±4.51	4.71
4.42	A	60 624	2.93±2.51	2.50
4.91	A	64 152	−3.03±2.53	2.56
5.21	D	221 298	−3.32±1.38	1.39
5.81	A	68 713	−1.08±2.44	2.47
6.25	B	173 181	−3.11±2.57	2.59
	C	128 196	−4.88±2.35	2.38
7.43	E	25 193	−2.96±0.73	0.73
9.57	E	28 259	−0.79±0.66	0.66
11.60	E	26 244	2.64±0.67	0.68

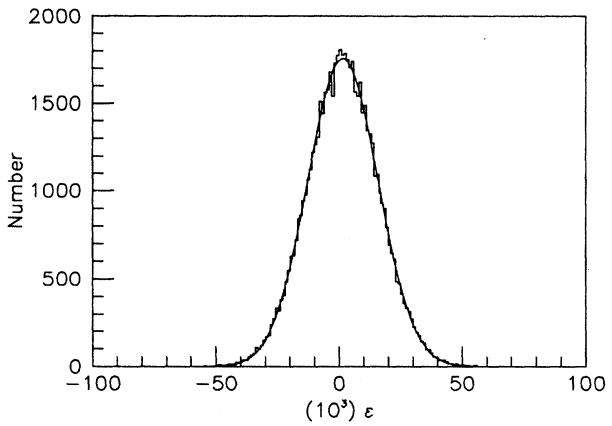

FIG. 6. Histogram of neutron transmission asymmetries for $E_n = 9.57$ MeV, target polarized. Each asymmetry represents 800 ms of data collection. The bin size is 1×10^{-3}. The smooth curve is the Poisson distribution predicted from counting statistics.

Average neutron transmission asymmetries $\bar{\varepsilon}_T$ are presented with statistical uncertainties in Tables III and IV for a polarized and unpolarized target, respectively. Also shown in these tables are N, the number of asymmetries included in the average, each corresponding to one eight-step sequence, and $\sigma_{\bar{\varepsilon}_T}$, the reduced standard deviation for the asymmetries. The excellent agreement between the statistical uncertainties and reduced standard deviations indicates that, primarily because of the fast spin-flip technique, the level of nonstatistical fluctuations is very small. Figure 6 is a histogram showing the agreement between the distribution of asymmetries and a calculated Gaussian curve.

The values of $\Delta\sigma_T$ calculated from Eqs. (23) and (24) are shown in Table V. The first uncertainty is statistical and is derived from the uncertainties in the asymmetries $\bar{\varepsilon}_T$. The second is systematic and is due to uncertainties in all other quantities in the equation, i.e., A_y, $K_y^{y'}$, etc. These results are plotted in Fig. 7. The error bars were obtained by adding the statistical and systematic uncertainties in quadrature. A zero-crossing energy of $E_{zc} = 5.08 \pm 0.10$ MeV was obtained by fitting the $\Delta\sigma_T$ values below 7 MeV.

TABLE V. Measured values of $\Delta\sigma_T$ with statistical and systematic uncertainties.

E_n (MeV)	$\Delta\sigma_T$ (mb)
3.65	253.7±27.9±26.8
4.42	44.7±34.4±4.4
4.91	41.0±33.6±3.5
5.21	−38.3±23.5±3.5
5.81	−25.8±29.1±2.8
6.25	−66.1±18.9±7.0
7.43	−129.0±10.6±5.3
9.57	−137.7±9.2±5.8
11.60	−147.2±10.1±5.4

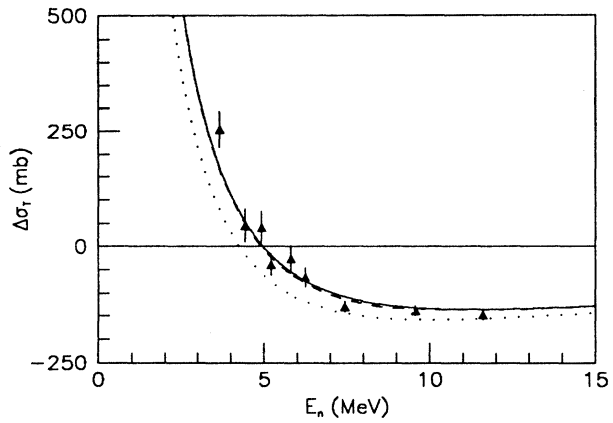

FIG. 7. Measured values of $\Delta\sigma_T$ compared to predictions from the PWA93 [5] (solid) phase-shift analysis, and the Bonn B [18] (dashed), and Paris [20] (dotted) potential models. The error bars represent the total uncertainty obtained by adding the statistical and systematic uncertainties in quadrature.

The results presented here differ in two ways from the preliminary results presented in Ref. [13]. First, the normalization cross section is different (see Sec. IV C) because of improvements in *NN* potential models and phase-shift analyses. Second, we incorrectly omitted the angle factor in Eq. (24) in the earlier analysis.

For completeness we show the various proton target and neutron beam polarizations in Tables VI and VII. The target polarizations are calculated from Eq. (17) using the calculated 1.94 MeV normalization cross section and the target thickness determined by weighing. The magnitude of the proton target polarization was typically $P_t = 0.38$. The neutron polarizations are calculated from Eq. (22). When using the ^{3}H(**p**,**n**)^{3}He source reaction, the magnitude of the neutron polarization was typically $P_n = 0.46$. When using the ^{3}H(**p**,**n**)^{3}He source reaction, the neutron polarization was substantially smaller. Because of a failed atomic transition unit, the deuteron beam polarization contained a large tensor component in one spin state. Because of this problem, we decided to turn the malfunctioning unit off, thus alternating between deuteron spin (−) and unpolarized.

VI. COMPARISON TO THEORETICAL PREDICTIONS

Figure 7 shows the measured values for $\Delta\sigma_T$ in comparison with potential model predictions and a recent *n-p* phase-shift analysis result. The agreement between the *n-p* potential model and phase-shift analysis curves and the data is very satisfactory. Table VIII lists the associated χ^2 values for a variety of potential models and phase-shift analyses. Figure 7 and Table VIII clearly demonstrate that a *NN* potential model (like Paris) fitted to the *p-p* scattering length in the *NN* $^1S_0$ interaction should not be used to describe the present *n-p* data.

In order to obtain values for the ϵ_1 mixing parameter from the $\Delta\sigma_T$ data, a phase-shift analysis is required. The analysis was performed by two separate methods. In the first, we started with the Nijmegen PWA93 phase-shift analysis and only varied the ϵ_1 parameter to reproduce the experimentally obtained $\Delta\sigma_T$ values. In the second, a full phase-shift analysis of the present data and all *n-p* data in the VPI database was performed simultaneously in the energy range of interest using the FORTRAN code NNF developed by the VPI group

TABLE VI. Proton target polarizations for each data set. The first uncertainty is statistical, while the second is systematic.

Set	P_t
A	−0.418±0.016±0.050
B	−0.309±0.016±0.039
C	−0.449±0.018±0.055
D	−0.327±0.014±0.040
E	0.377±0.014±0.044

TABLE VII. Neutron beam polarizations for each neutron transmission asymmetry measurement.

E_n (MeV)	Set	Target polarized P_n	Target unpolarized P_n
1.94	*A*	0.496±0.030	0.439±0.031
	B	−0.438±0.034	
	C	−0.454±0.032	−0.436±0.034
	D_1	−0.399±0.028	−0.444±0.031
	D_2	−0.298±0.017	
3.65	*C*	−0.471±0.033	−0.468±0.032
	D	−0.372±0.025	−0.444±0.031
4.42	*A*	0.439±0.028	0.468±0.030
4.91	*A*	0.532±0.023	0.472±0.021
5.21	D_1	−0.310±0.011	−0.460±0.016
	D_2	−0.440±0.015	
5.81	*A*	0.547±0.020	0.491±0.017
6.25	*B*	−0.559±0.036	−0.545±0.035
	C	−0.592±0.038	−0.563±0.036
7.43	*E*	0.301±0.010	0.308±0.011
9.57	*E*	0.325±0.006	0.324±0.006
11.60	*E*	0.318±0.007	0.318±0.008

TABLE VIII. χ^2/N_{data} values resulting from comparing the present $\Delta\sigma_T$ data to predictions from potential models and phase-shift analyses.

	χ^2/N_{data}
Argonne AV18[a]	1.30
Bonn B[b]	1.27
Full Bonn[c]	1.40
Nijmegen Nijm93[d]	1.39
Nijmegen PWA93[e]	1.36
Paris[f]	5.93
VPI SM94[g]	1.30

[a]Reference [21].
[b]Reference [18].
[c]Reference [17].
[d]Reference [2].
[e]Reference [5].
[f]Reference [20].
[g]Reference [6].

TABLE IX. Values of the ϵ_1 mixing parameter obtained from the data by a single-parameter phase-shift analysis. All other phases are taken from the Nijmegen PWA93 phase-shift analysis [5].

E_n (MeV)	ϵ_1 (deg)
5.08	0.48±0.22
7.43	1.57±0.36
9.57	1.36±0.41
11.60	1.37±0.52

[36]. In the full analysis, all phase-shift parameters for $J \leq 1$ were allowed to vary, starting with the VZ40 solution [6] of the VPI group, with the exception of the $^1P_1$ phase shift. The VZ40 solution differs from the SM94 solution as it is restricted to the energy range 0–400 MeV, while SM94 covers the range 0–1.3 GeV. The $^1P_1$ phase-shift parameter was not varied because $\Delta\sigma_T$ has almost no sensitivity to its value, and there are no other n-p data in the energy region of interest to fix its value.

The values of the ϵ_1 mixing parameter obtained in the single-parameter phase-shift analysis are listed in Table IX and plotted in Fig. 8 as solid triangles. Table X lists phase shifts obtained in the full analysis along with χ^2 values for both n-p and p-p data. The ϵ_1 values obtained from the two analyses are consistent.

Figure 8 summarizes the experimental and theoretical situation with respect to ϵ_1 in the energy region below 60 MeV. Our values for ϵ_1 are in very good agreement with both the Nijmegen PWA93 and the VPI VZ40 phase-shift analysis results, and with the Bonn B potential-model predictions. The trend of our data for ϵ_1 brings into question the reliability of the ϵ_1 values at 13.7 and 17.4 MeV. The value quoted at 13.7 MeV (square) was taken from Ref. [37]. We performed a single-parameter phase-shift analysis to obtain a value for ϵ_1 from the $K_y^{y'}$ result reported in Ref. [38] (circle). Clearly, data above 12 MeV are needed to clarify this situation. Figure 8 also shows that accurate data are required to settle the issue raised by the difference between the VZ40 and PWA93 phase-shift analysis results above 20 MeV. As has been shown by Machleidt and Slaus [11], realistic meson-exchange based NN potential models cannot yield

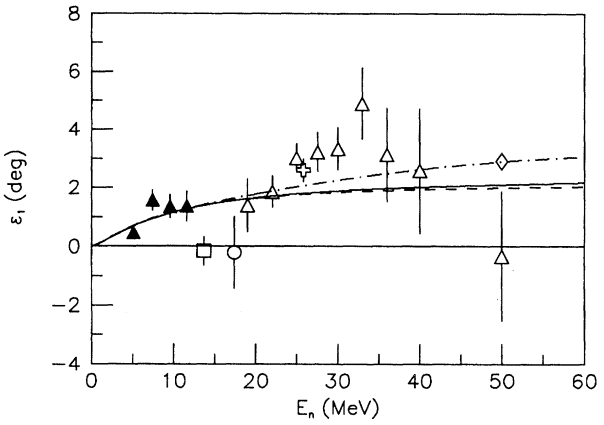

FIG. 8. Values of ϵ_1 obtained from analysis of experimental data compared to predictions from the PWA93 [5] (solid) and VZ40 [6] (dot-dashed) phase-shift analyses, and the Bonn B [18] (dashed) potential model. The data are from the single-parameter phase-shift analysis of the present work (solid triangles), and from previous work as discussed in the text.

values for ϵ_1 as large as the two data shown in Fig. 8 at 25.8 [39] (cross) (obtained from a single $K_y^{y'}$ datum) and 50 MeV [12] (diamond) [obtained mainly from zero-crossing data of $A_{zz}(\theta)$]. Although details related to the n-p A_{yy} data [40] measured at Karlsruhe some 10 years ago have not been published, we took their $A_{yy}(\theta)$ data at $\theta_{\text{c.m.}}=90°$ [41] and, again using the Nijmegen PWA93 phase-shift analysis, ϵ_1 was modified to reproduce the measured $A_{yy}(90°)$ data between 19 and 50 MeV. The associated values for ϵ_1 are given in Fig. 8 as open triangles. The Karlsruhe results between 25 and 33 MeV clearly support the large values found for ϵ_1 at 25.8 and 50 MeV. If confirmed, this could have serious consequences for all present NN potential models. Therefore, we recommend new experimental determinations of ϵ_1 between 15 and 50 MeV to investigate the present disagreement between data and calculations near 15 MeV and to resolve the discrepancy between VZ40 on one side and PWA93 and realistic NN potential models on the other side.

TABLE X. Values of the $J=0$ and 1 phase-shift parameters obtained in the full phase-shift analysis. The values in parentheses were not varied. N_{pp} and N_{np} are the number of p-p and n-p data. χ^2_ν is the reduced χ^2.

	5.08 MeV (4.08–6.08 MeV)	7.43 MeV (5.43–9.43 MeV)	9.57 MeV (7.57–11.57 MeV)	11.60 MeV (9.60–13.60 MeV)
$^1S_0$	62.26±0.10	60.60±0.08	58.35±0.11	58.20±0.11
$^3P_0$	1.55±0.10	3.01±0.13	3.33±0.04	4.17±0.04
$^1P_1$	(−1.41)	(−2.11)	(−2.69)	(−3.20)
$^3P_1$	−0.88±0.03	−1.68±0.07	−1.86±0.02	−2.33±0.02
$^3S_1$	118.03±0.15	109.45±0.27	103.83±0.34	100.00±0.65
ϵ_1	0.09±0.23	1.17±0.37	0.72±0.42	1.06±0.52
$^3D_1$	−1.40±1.74	−0.34±0.03	−0.57±0.02	−0.82±0.02
χ^2/N_{pp}	25.02/28	52.53/34	80.75/88	85.77/81
χ^2/N_{np}	42.98/45	19.85/25	37.19/51	57.80/49
χ^2_ν	1.01	1.37	0.89	1.16

VII. CONCLUSIONS

We have reported measurements of the polarized neutron, polarized proton transverse cross-section difference, $\Delta\sigma_T$, in the energy range 3.65–11.60 MeV. At these energies $\Delta\sigma_T$ is particularly sensitive to the poorly known *NN* phase-shift parameter ϵ_1, the $^3S_1-^3D_1$ tensor mixing parameter. We report two separate phase-shift analyses of the data, and, in contrast to work at higher energies, we find ϵ_1 values in good agreement with the predictions of *NN* potential models.

While the agreement with the potential models below 12 MeV is gratifying, the disagreements above this energy (small ϵ_1 values at 13.6 and 17.4 MeV and large between 25 and 50 MeV) remain to be understood. A particular issue is that the value of ϵ_1 extracted depends on the values of other *NN* force components, in particular, the singlet phase-shift parameter $^1S_0$. Different values of this parameter are found from analysis of *p-p* and *n-p* scattering data. We show that an almost unique determination of ϵ_1 can be made if both longitudinal and transverse cross-section differences are determined because the difference between $\Delta\sigma_T$ and $\Delta\sigma_L$ is completely insensitive to all singlet phase-shift parameters. An experiment to measure $\Delta\sigma_L$ is currently being prepared at TUNL.

ACKNOWLEDGMENTS

The authors wish to thank R. A. Arndt and I. I. Strakovsky for their help with the analysis code. We thank H. O. Klages for the high-purity TiH_2, without which the experiment would not have been possible. We are grateful to J. E. Koster for his assistance during the early part of the experiment. This work was supported in part by the U.S. Department of Energy, Office of High Energy and Nuclear Physics, under Grant Nos. DEFG05-91ER40619 and DEFG05-88ER40441.

[1] R. Machleidt and G. Q. Li, Phys. Rep. **242**, 5 (1994).
[2] V. G. J. Stoks, R. A. M. Klomp, C. P. F. Terheggen, and J. J. de Swart, Phys. Rev. C **49**, 2950 (1994).
[3] F. Myhrer and J. Wroldsen, Rev. Mod. Phys. **60**, 629 (1988).
[4] M. Fukugita, Y. Kuramashi, H. Mino, M. Okawa, and A. Ukawa, Phys. Rev. Lett. **73**, 2176 (1994).
[5] V. G. J. Stoks, R. A. M. Klomp, M. C. M. Rentmeester, and J. J. de Swart, Phys. Rev. C **48**, 792 (1993).
[6] R. A. Arndt, I. I. Strakovsky, and R. L. Workman, Phys. Rev. C **50**, 2731 (1994).
[7] R. Binz *et al.*, Nucl. Phys. **A508**, 267c (1990).
[8] P. Haffter *et al.*, Nucl. Phys. **A548**, 29 (1992).
[9] R. Henneck, Phys. Rev. C **47**, 1859 (1993).
[10] G. E. Brown and R. Machleidt, Phys. Rev. C **50**, 1731 (1994).
[11] R. Machleidt and I. Slaus, Phys. Rev. Lett. **72**, 2664 (1994).
[12] M. Hammans *et al.*, Phys. Rev. Lett. **66**, 2293 (1991).
[13] W. S. Wilburn, C. R. Gould, D. G. Haase, P. R. Huffman, C. D. Keith, J. E. Koster, N. R. Roberson, and W. Tornow, Phys. Rev. Lett. **71**, 1982 (1993).
[14] D. V. Bugg, J. Phys. G **6**, 1329 (1980).
[15] W. Tornow, Bull. Am. Phys. Soc. **33**, 1582 (1988).
[16] W. Tornow, O. K. Baker, C. R. Gould, D. G. Haase, N. R. Roberson, and W. S. Wilburn, in *Physics with Polarized Beams and Polarized Targets*, edited by J. Sowinski and S. E. Vigdor (World Scientific, Singapore, 1989), p. 75.
[17] R. Machleidt, K. Holinde, and C. Elster, Phys. Rep. **149**, 1 (1987).
[18] R. Machleidt, Adv. Nucl. Phys. **19**, 189 (1989).
[19] G. A. Miller, B. M. K. Nefkens, and I. Slaus, Phys. Rev. **194**, 1 (1990).
[20] M. Lacombe, B. Loiseau, J. M. Richard, R. Vinh Mau, J. Côté, P. Pirès, and R. de Tourreil, Phys. Rev. C **21**, 861 (1980).
[21] R. B. Wiringa, V. G. J. Stoks, and R. Schiavilla, Phys. Rev. C **51**, 38 (1995).
[22] D. G. Haase, C. R. Gould, and L. W. Seagondollar, Nucl. Instrum. Methods Phys. Res., Sect. A **243**, 305 (1986).
[23] R. Aures, W. Heering, H. O. Klages, R. Maschuw, F. K. Schmidt, and B. Zeitnitz, Nucl. Instrum. Methods **224**, 347 (1984).
[24] W. Heeringa, R. Aures, R. Maschuw, and F. K. Schmidt, Cryogenics **25**, 369 (1985).
[25] C. D. Keith, C. R. Gould, D. G. Haase, N. R. Roberson, W. Tornow, and W. S. Wilburn, Hyperfine Interact. **75**, 525 (1992).
[26] T. B. Clegg *et al.*, Nucl. Instrum. Methods Phys. Res., Sect. A **357**, 200 (1995).
[27] S. J. Moss and W. Haeberli, Nucl. Phys. **72**, 417 (1965).
[28] G. E. Terrell, M. F. Jahns, M. R. Kostoff, and E. M. Bernstein, Phys. Rev. **173**, 931 (1968).
[29] T. R. Donoghue, R. C. Haight, G. P. Lawrence, J. E. Simmons, D. C. Dodder, and G. M. Hale, Phys. Rev. Lett. **27**, 947 (1971).
[30] J. E. Simmons, J. E. Simmons, W. B. Broste, T. R. Donoghue, R. C. Haight, and J. C. Martin, Nucl. Instrum. Methods **106**, 477 (1973).
[31] W. S. Wilburn, C. R. Gould, D. G. Haase, P. R. Huffman, C. D. Keith, N. R. Roberson, and W. Tornow (unpublished).
[32] W. Tornow, Z. Phys. **266**, 357 (1974).
[33] Link Analytical Limited, Bucks, England.
[34] N. R. Roberson *et al.*, Nucl. Instrum. Methods Phys. Res., Sect. A **326**, 549 (1993).
[35] J. M. Blatt and L. C. Biedenharn, Phys. Rev. **86**, 399 (1952).
[36] R. A. Arndt, J. S. Hyslop III, and L. D. Roper, Phys. Rev. D **35**, 128 (1987).
[37] M. Schöberl, H. Kuiper, R. Schmelzer, G. Mertens, and W. Tornow, Nucl. Phys. **A489**, 284 (1988).
[38] M. Ockenfels, T. Köble, M. Schwindt, J. Weltz, and W. von Witsch, Nucl. Phys. **A534**, 248 (1991).
[39] M. Ockenfels, F. Meyer, T. Köble, W. von Witsch, J. Weltze, K. Wingender, and G. Wollmann, Nucl. Phys. **A526**, 109 (1991).
[40] P. Doll, V. Eberhard, G. Fink, R. W. Finlay, T. D. Ford, W. Heeringa, H. O. Klages, H. Krupp, and Chr. Wölfl, in *Few Body XII*, edited by B. K. Jennings (TRIUMF, Vancouver, 1989), p. C16.
[41] C. Wölfl, Ph.D. thesis, Universität Karlsruhe, 1988.